



1 **Technical note: 12-km resolution capability for the global GEOS-Chem model of atmospheric
2 composition**

3 Xiaolin Wang¹, Melissa P. Sulprizio¹, Yuyao Zhuge², Randall V. Martin², Daniel J. Jacob¹

4 ¹ School of Engineering and Applied Sciences, Harvard University, Cambridge, MA, USA

5 ² Department of Energy, Environmental & Chemical Engineering, Washington University in St.
6 Louis, St. Louis, MO, USA

7

8 *Correspondence to:* Xiaolin Wang (wangxi@g.harvard.edu)

9

10

11 **Abstract**

12

13 We present a new 12-km nested resolution capability in the GEOS-Chem global model of
14 atmospheric composition. This capability can be applied to simulations for any user-selected
15 domain worldwide from March 2021 onward by accessing a new hourly cubed-sphere C720
16 ($\approx 0.125^\circ \times 0.15625^\circ$ or $12 \times 12 \text{ km}^2$) global wind archive from the NASA GEOS-FP
17 meteorological data assimilation system. We evaluate this 12-km configuration of GEOS-Chem
18 by comparison with the standard 25-km nested configuration in simulations of transport tracers,
19 oxidant-aerosol chemistry, and inversions of satellite data using the Integrated Methane Inversion
20 (IMI). The 12-km simulation features stronger vertical transport (up to 20% lower surface ^{222}Rn
21 concentrations) because it better captures eddy fluxes both spatially and temporally. Aerosol
22 deposition and stratosphere–troposphere exchange are similar at the two resolutions. The 12-km
23 oxidant-aerosol chemistry can better simulate urban observations of NO_2 , with stronger ozone
24 urban titration but slightly higher surface ozone background due to enhanced vertical transport.
25 12-km and 25-km inversions using the IMI show highly consistent results on the regional scale,
26 but the 12-km inversion provides greater information and improved spatial detail to resolve
27 emissions from different sectors.

28

29 **1. Introduction**

30 GEOS-Chem (<http://geos-chem.org>) is an open-source global 3-D model of atmospheric
31 chemistry originally described by Bey et al. (2001) and used by hundreds of research groups
32 around the world for a wide range of applications. It is driven by archived Goddard Earth
33 Observing System (GEOS) meteorological data from the NASA Global Modeling and
34 Assimilation Office (GMAO). Here we introduce the capability to conduct GEOS-Chem
35 simulations at $0.125^\circ \times 0.15625^\circ$ ($\approx 12 \times 12 \text{ km}^2$) resolution by exploiting a new GEOS advection
36 data archive combined with the nested capability of GEOS-Chem. This enables low-cost,
37 reproducible, high-resolution simulations of atmospheric chemistry and air quality anywhere in



38 the world and for any period from March 2021 onward. In what follows we will refer to it as the
39 12-km capability in GEOS-Chem.

40 The open-access GEOS global meteorological datasets used to drive GEOS-Chem are produced
41 at GMAO by data assimilation on the cubed-sphere grid of the underlying GEOS Earth system
42 model (ESM) and then archived on a rectilinear latitude-longitude grid for public dissemination.
43 The GEOS-Chem Support Team extracts from these archives the data needed to run GEOS-
44 Chem and distributes them to users as an open dataset library through the Amazon Web Services
45 (AWS) cloud (Zhuang et al., 2019; Martin et al., 2022). GEOS-Chem users may choose from
46 three main datasets: the Modern-Era Retrospective Analysis for Research and Applications,
47 version 2 (MERRA-2; 1980-present) at $0.5^\circ \times 0.625^\circ$ resolution, the GEOS Forward Processing
48 (GEOS-FP; 2014-present) at $0.25^\circ \times 0.3125^\circ$ resolution, and the GEOS for Instrument Teams
49 (GEOS-IT; 1998-present) at $0.5^\circ \times 0.625^\circ$ resolution or native cubed-sphere C180 resolution (180
50 grid cells per cubed-sphere side, corresponding to $\approx 0.5^\circ \times 0.625^\circ$ resolution). MERRA-2 provides
51 a long stable record with fixed physics and data assimilation algorithms, GEOS-IT is the next-
52 generation stable record with updated physics and data assimilation, and GEOS-FP is the
53 operational product generated in near real time using the latest validated GEOS system. GEOS-
54 FP operates at native C720 resolution ($\approx 0.125^\circ \times 0.15625^\circ$) but the data archive was previously
55 made available only at $0.25^\circ \times 0.3125^\circ$ resolution. Since March 2021, GMAO has been producing
56 a native-resolution hourly C720 GEOS-FP advection archive specifically to serve GEOS-Chem
57 needs, and this is what we use to enable the 12-km capability in GEOS-Chem.

58 GEOS-Chem operates in two modes, Classic (GC-Classic) and High-Performance (GCHP)
59 (Martin et al., 2022). GC-Classic is designed for easy use on the rectilinear longitude-latitude
60 grid and operates on single-node mode with shared-memory parallelization. GCHP enables high-
61 resolution simulations using distributed-memory parallelization (MPI) on the cubed sphere with
62 efficient multi-node scalability extending to thousands of cores (Eastham et al., 2018). Both GC-
63 Classic and GCHP can operate on the native GEOS grid resolutions but also at coarser
64 resolutions for computational economy using regridded GEOS data archived on AWS as part of
65 the GEOS-Chem input dataset library. Global GC-Classic simulations thus typically use $2^\circ \times$
66 2.5° or $4^\circ \times 5^\circ$ GEOS data. GC-Classic includes a one-way nested capability to conduct native-
67 resolution simulations over limited domains with archived dynamic boundary conditions from a
68 coarse-resolution simulation (Wang et al., 2004). GCHP includes a stretched-grid capability to
69 enable higher-resolution two-way nesting over target regions (Bindle et al., 2021). Emission and
70 surface type information are generally available at $0.1^\circ \times 0.1^\circ$ (≈ 10 -km) resolution from the
71 GEOS-Chem input dataset library, from which they are regridded on the fly within GEOS-Chem
72 at the desired resolution using the HEMCO software tool (Lin et al., 2021). The one-way nested
73 GC-Classic capability at GEOS-FP $0.25^\circ \times 0.3125^\circ$ (≈ 25 -km) resolution is widely used for air
74 quality applications (Kim et al., 2015; Zhang et al., 2015) and for inversions of greenhouse gas
75 data to infer surface fluxes (Varon et al., 2022).



76 Here, we implement the GEOS-FP native C720 advection archive for use in GC-Classic nested-
77 grid simulations. This 12-km capability can be applied over any user-selected domain
78 worldwide, and for any period from March 2021 onward. It has been released in GEOS-Chem
79 version 14.6.0 (<https://doi.org/10.5281/zenodo.15243271>). We describe the 12-km capability in
80 Section 2 and compare its transport to the standard 25-km nested GC-Classic configuration in
81 Section 3. We then demonstrate its application to a full-chemistry simulation over the North
82 China Plain (Section 4) and to the inversion of satellite observations using the Integrated
83 Methane Inversion (IMI) framework (Section 5).

84 **2. GEOS-Chem simulation at 12-km resolution**

85 GC-Classic allows users to conduct nested simulations over any domain of interest using the
86 GEOS meteorological archives as input and with rectilinear coordinates specified at runtime.
87 This framework was first introduced by Wang et al. (2004) and updated to $0.25^\circ \times 0.3125^\circ$
88 resolution by Zhang et al. (2015) and Kim et al. (2015). The nested simulations are conducted as
89 a regional model with boundary conditions provided by a separate global simulation at $2^\circ \times 2.5^\circ$
90 or $4^\circ \times 5^\circ$ resolution that provides dynamic chemical fields updated every three hours.

91 Here we use the new global C720 GEOS-FP hourly advection archive, regridded to $0.125^\circ \times$
92 0.15625° , to enable GC-Classic nested-grid simulations at 12-km resolution. Table 1 summarizes
93 the GEOS-FP input data for the 12-km configuration as compared to the 25-km configuration.
94 The idea behind the advection archive is that higher resolution is most needed for the winds to
95 better represent eddy flows and to leverage the $0.1^\circ \times 0.1^\circ$ resolution of the emission data.
96 Limiting the number of variables in the advection archive enables global computational storage
97 at C720. Other non-advection meteorological inputs including convective mass fluxes and
98 vertical mixing depths are from the standard GEOS-FP archive at $0.25^\circ \times 0.3125^\circ$ resolution and
99 are dynamically regridded to $0.125^\circ \times 0.15625^\circ$ on the fly during the 12-km simulation. Most
100 emission datasets are available on a $0.1^\circ \times 0.1^\circ$ grid and are regridded on the fly to the simulation
101 resolution using HEMCO (Lin et al., 2021).

102 The 12-km advection archive includes horizontal wind vectors, surface pressure, and specific
103 humidity on 72 vertical levels extending from the surface to 0.01 hPa (model top). Surface
104 pressure is needed to infer the vertical air mass fluxes from the horizontal air mass fluxes by
105 mass conservation. Specific humidity is needed to convert wet air fluxes and pressure in the
106 GEOS data to dry air fluxes and pressures used in GEOS-Chem. The 12-km advection archive
107 has hourly temporal resolution, compared to 3-hourly resolution for the 3-D variables in the 25-
108 km archive. We maintain separate 12-km advection archives for five continental regions (Africa,
109 Asia, Europe, North America, and South America) to reduce data size and thereby speed up data
110 access and processing over the user-selected nested domains
111 (<https://registry.opendata.aws/geoschem-nested-input-data>).



112 All simulations presented here were carried out on the Harvard Cannon v2.0 supercomputing
113 cluster using compute nodes equipped with dual-socket Intel Xeon Platinum 8480CL CPUs (56
114 cores each, base frequency \sim 2.9 GHz). Each simulation used 48 physical CPU cores and ran on a
115 single node. We find that the 12-km simulation wall-time is about 7 \times that of a 25-km simulation
116 over the same domain. This is driven by the 4 \times increase in grid cells and the 2 \times reduction in
117 timestep. The 1-month full-chemistry simulation presented in Section 4 took 26 wall-time hours
118 to complete at 12-km resolution.

119

120 **Table 1.** GEOS-FP meteorological data archives available for driving GEOS-Chem^a.

GEOS-Chem simulation	12 \times 12 km 2	25 \times 25 km 2
Archive period	March 2021-present	January 2014-present
Horizontal resolution (advection)	0.125 $^{\circ}$ \times 0.15625 $^{\circ}$	0.25 $^{\circ}$ \times 0.3125 $^{\circ}$
Temporal resolution (advection)	Hourly	3-hourly
Horizontal resolution (other)	0.25 $^{\circ}$ \times 0.3125 $^{\circ}$ regridded to 0.125 $^{\circ}$ \times 0.15625 $^{\circ}$	0.25 $^{\circ}$ \times 0.3125 $^{\circ}$
Temporal resolution (other)	3-hourly or hourly ^b	3-hourly or hourly
Timestep ^c	Transport 150 s Non-transport 300 s	Transport 300 s Non-transport 600 s

121 a. For GC-Classic simulations at 0.125 $^{\circ}$ \times 0.15625 $^{\circ}$ and 0.25 $^{\circ}$ \times 0.3125 $^{\circ}$ resolutions (\approx 12 \times 12
122 km 2 and 25 \times 25 km 2) with 72 hybrid sigma-pressure vertical levels extending up to 0.01
123 hPa. GEOS-FP meteorological data used as GEOS-Chem input include advection
124 variables (horizontal wind vectors, surface pressure, specific humidity) and other
125 variables driving convective transport, planetary boundary layer (PBL) mixing,
126 emissions, radiation, chemistry, and deposition. The full list of variables is at:
127 [135](https://wiki.seas.harvard.edu/geos-chem/index.php>List_of_GEOS-FP_met_fields. The
128 advection variables are grouped in a separate advection archive for 12-km applications.
129 The 12-km and 25-km archives are available globally, and also for individual continents
130 to speed up data extraction.</p><p>131 b. Hourly for two-dimensional fields such as surface properties and PBL depth; 3-hourly for
132 three-dimensional fields such as temperature and convective mass flux.</p><p>133 c. Recommended timesteps for operator splitting (Philip et al., 2016), can be adjusted by
134 user. Non-transport operators include emissions, chemistry, and deposition.</p></div><div data-bbox=)



136 3. Transport tracer simulations

137 We use the TransportTracers simulation of GEOS-Chem (https://wiki.seas.harvard.edu/geos-chem/index.php/TransportTracers_simulation) to evaluate model transport and scavenging
138 processes. This simulation includes 21 generic species (tracers) to test the different components
139 of GEOS-Chem transport. We focus here on the radionuclide tracers radon-222 (^{222}Rn), lead-210
140 (^{210}Pb), and beryllium-7 (^7Be), which are routinely used to benchmark transport and wet
141 deposition in GEOS-Chem (Liu et al., 2001; Yu et al., 2018). The nested-grid simulations are
142 conducted over Eastern China (100–125°E, 17–45°N, domain shown in Figure 1) at both
143 $0.125^\circ \times 0.15625^\circ$ and $0.25^\circ \times 0.3125$ resolutions for February and June 2022. Initial conditions are
144 generated from spin-up simulations at the same resolutions, starting from October 2021
145 (corresponding to spin-up periods of 4 months for February and 8 months for June). The
146 boundary conditions are updated every three hours from a global simulation at $2^\circ \times 2.5^\circ$
147 resolution.
148

149 Figure 1 shows surface ^{222}Rn concentrations from the 12-km simulation and relative differences
150 with the 25-km simulation. ^{222}Rn in the simulation has a uniform soil source and is removed by
151 radioactive decay with a half-life of 3.8 days, making it a sensitive tracer for vertical transport in
152 the troposphere (Liu et al., 2001; Yu et al., 2018). Surface ^{222}Rn concentrations are lower by 0–
153 20% at 12-km than at 25-km resolution. The total ^{222}Rn burden in the two simulations is the
154 same, and the difference is in the vertical distribution (Figure 2). The 12-km simulation shows
155 reduced ^{222}Rn in the lower troposphere and enhanced concentrations in the middle-upper
156 troposphere, indicating stronger vertical transport. Differences are most pronounced over
157 complex terrain such as Sichuan and Taiwan.
158

159 Transport processes in GEOS-Chem include grid-resolved advection (winds), sub-grid
160 parameterized convection (convective mass fluxes), and PBL-mixing (Lin and McElroy, 2010).
161 We find that the differences between the 12-km and 25-km simulations persist even when
162 convection and PBL mixing (both from the 25-km archive) are shut off. The enhanced vertical
163 transport at 12-km is thus driven by the improved resolution of advection, both spatially and
164 temporally (1-hour versus 3-hour). When winds are averaged in space and time relative to the
165 parent GEOS ESM simulation (here at C720 with 7.5 minutes timesteps), vertical eddy fluxes are
166 lost. This has been recognized previously as a major driver of differences between GEOS-Chem
167 simulations at different resolutions (Yu et al., 2018). The 12-km simulation has no spatial
168 averaging of winds relative to the parent GEOS ESM and only 1-hour temporal averaging, and
169 therefore retains more of the native GEOS ESM vertical motions to produce stronger vertical
170 eddy fluxes of ^{222}Rn .

171 ^{210}Pb (half-life of 22.3 years) is produced by the decay of ^{222}Rn , and ^7Be (half-life of 53.3 days)
172 is generated by cosmic-ray interactions with atmospheric oxygen and nitrogen at high altitudes.
173 Both radionuclides rapidly attach to aerosol particles and are subsequently transported and



173 removed by wet and dry deposition. This makes ^{210}Pb useful to evaluate aerosol transport and
174 removal processes, with ^7Be providing complementary information on stratosphere–troposphere
175 exchange and tropospheric subsidence (Liu et al., 2001). Comparisons of 12-km and 25-km
176 simulations for ^{210}Pb show similar differences as for ^{222}Rn (Figure 2) but weaker in magnitude
177 because the ^{210}Pb source is more diffuse. Lifetimes against deposition differ by less than 2%
178 between the 12-km and 25-km simulations. Comparisons for ^7Be also show weaker differences
179 than for ^{222}Rn because vertical transport of ^7Be in the troposphere is mainly by large-scale
180 subsidence, which is less sensitive to eddy motions. We find no significant difference in
181 transport of ^7Be across the tropopause.

182

183 **4. Full-chemistry simulations**

184 We perform 1-month full-chemistry simulations for February and June of 2022 over the North
185 China Plain (domain shown in Figure 3) at 12-km and 25-km horizontal resolutions for
186 comparison. The full-chemistry configuration of GEOS-Chem includes detailed ozone–NO_x–
187 VOCs–aerosol–halogen tropospheric and stratospheric chemistry (Wang et al., 2021). Boundary
188 conditions are provided by a global $2^\circ \times 2.5^\circ$ GEOS-Chem simulation and updated every three
189 hours, and spin-up simulations are conducted from October 2021 to generate initial conditions.
190 Monthly anthropogenic emissions are from the MIXv2 Asian emission inventory at $0.1^\circ \times 0.1^\circ$
191 resolution for 2017, scaled to 2022 using province-level emission data from the MEIC v1.4
192 inventory (Zheng et al., 2018) and mapped to the 12-km and 25-km grids using HEMCO. We
193 compare the model simulations of surface NO₂, ozone, and fine particulate matter (PM_{2.5})
194 concentrations to hourly observations from 361 sites operated by the China National
195 Environmental Monitoring Centre (CNEMC; <http://www.cnemc.cn>, last assess: 23 May 2023).
196 The sites are mainly urban. We remove anomalous observations at each site following the quality
197 control protocols described in Lu et al. (2018). We sample model outputs at the observation sites
198 for comparisons.

199 Figure 3 shows the afternoon (13–18 local time) surface NO₂ concentrations over the NCP in
200 June 2022 and the effect of model resolution. The finer structure at 12-km resolution is evident
201 and largely reflects the ability to exploit the higher resolution of emissions. Comparison to
202 CNEMC observations (Figure 4a) shows a low bias in the model, likely reflecting the near-
203 source locations of the sites, but the bias is reduced at 12-km resolution. The 12-km simulation
204 does not improve the correlation with observations for individual CNEMC sites, which could
205 reflect errors in model transport or in the spatial distribution of emissions.

206 Figure 5 compares simulated maximum daily 8-h average (MDA8) surface ozone concentrations
207 at 12-km and 25-km resolutions in June 2022. The differences between the two resolutions are
208 generally smaller than 5 ppb, and there is no significant difference in the fit to observations
209 (Figure 4b). Background ozone concentrations increase by up to 3 ppb over the northern NCP



210 region, likely driven by increased vertical transport of ozone from aloft as seen in the simulated
211 ^{77}Be concentrations in Figure 1. Increasing the model resolution to 12-km decreases surface
212 ozone concentrations by about 3 ppb in Beijing and 6 ppb in Tianjin city core areas, as expected
213 from higher NO_x concentrations driving stronger ozone titration, whereas suburban areas exhibit
214 ozone increases of no more than 2 ppb. These effects are too small to be effectively evaluated in
215 the comparison to observations (Figure 4b).

216 Figures 6 shows the daily-averaged total $\text{PM}_{2.5}$ mass concentrations in February 2022, where
217 $\text{PM}_{2.5}$ is computed in the model as the sum of fine aerosol components (Zhai et al., 2021). We
218 focus on February here because $\text{PM}_{2.5}$ concentrations are higher in winter than in summer (Zhai
219 et al., 2019). $\text{PM}_{2.5}$ concentrations are in general slightly lower at 12-km resolution because of
220 the enhanced vertical transport. However, higher concentrations are found in a few urban
221 hotspots due to primary organic aerosol emissions from combustion that are better resolved.
222 Again, differences are too small to be arbitrated by the observations (Figure 4c).

223

224 **5. Application to the Integrated Methane Inversion (IMI)**

225 The IMI applies the nested GEOS-Chem as forward model in regional analytical inversions of
226 TROPOMI satellite observations of methane columns to optimize methane emissions (Estrada et
227 al., 2025; Varon et al., 2022). The TROPOMI satellite observations are at $5.5 \times 7 \text{ km}^2$ pixel
228 resolution so there is potential benefit for conducting the inversion at 12-km resolution using our
229 new GEOS-Chem capability. The 12-km IMI configuration was previously applied in Wang et al.
230 (2025) to quantify methane emissions across 12 U.S. urban areas. Here we examine how
231 inversion results vary between 12-km and 25-km resolution, focusing on the Houston urban area
232 in eastern Texas as an example.

233 The IMI inversion procedure is described by Estrada et al. (2025) and Hancock et al. (2025),
234 including the design of state vector, error estimates, and optimization strategy. Here we optimize
235 annual methane emissions in 2022 over a $3^\circ \times 4^\circ$ (latitude \times longitude) domain encompassing
236 Houston and its surrounding area as shown in Figure 7. The state vector to be optimized consists
237 of emissions in each land-containing grid cell of the $3^\circ \times 4^\circ$ domain (496 elements at 12-km
238 resolution and 164 elements at 25-km resolution) and boundary conditions on each lateral edge
239 (4 elements). Our prior estimates of anthropogenic emissions are from the U.S. Environmental
240 Protection Agency Greenhouse Gas Inventory (GHGI) at $0.1^\circ \times 0.1^\circ$ resolution for 2020
241 (Maasakkers et al., 2023). Natural emissions follow the default configuration as described in
242 Estrada et al. (2025). We assume a lognormal prior error probability density function (PDF) for
243 emissions with a geometric error standard deviation of 2.0 (Bruno et al., 2025), and a normal
244 error PDF for boundary conditions with a 10 ppb error standard deviation. The IMI analytical
245 inversion returns optimized (posterior) emissions and a posterior error covariance matrix from



246 which the averaging kernel matrix can be derived as a measure of information content from the
247 observations (Brasseur and Jacob, 2017).

248 The prior estimate of total emissions over the $3^\circ \times 4^\circ$ inversion domain is 790 Gg a⁻¹ (Figure 7).
249 Total posterior emissions are 50% higher than the prior estimate and agree closely between the
250 12-km inversion (1260 Gg a⁻¹) and the 25-km inversion (1170 Gg a⁻¹). The 12-km inversion
251 results, when averaged over the 25-km grid, show a high degree of consistency with the 25-km
252 inversion results over the inversion domain (spatial correlation coefficient = 0.92). The trace of
253 the averaging kernel matrix defines the Degrees of Information for Signal (DOFS) indicating the
254 number of pieces of information that can be obtained from the observations through the inversion
255 independently from the prior estimate. The DOFS for the $3^\circ \times 4^\circ$ domain is 24.4 for the 12-km
256 inversion, higher than the 16.8 for the 25-km inversion. Conducting the inversion at higher
257 resolution allows for more information on emissions to be extracted from the observations.

258 Another advantage of the higher-resolution inversion is better separation of the sectors
259 contributing to methane emissions. Sectoral information in the inversion is obtained by
260 attributing the posterior/prior emission ratios for each grid cell to the different sectors
261 contributing emissions to that grid cell in the prior estimate (Wecht et al., 2014). Higher spatial
262 resolution in the inversion reduces spatial overlap between sectors.

263 In summary, we have implemented a 12-km resolution nested capability in the GEOS-Chem
264 global model of atmospheric chemistry by taking advantage of a new hourly GEOS advection
265 archive available globally from March 2021 onward and freely distributed to GEOS-Chem users
266 through the AWS cloud. We compared the 12-km simulation to the standard 25-km nested
267 simulation in GEOS-Chem for transport tracers (^{222}Rn , ^{210}Pb , ^7Be), ozone-aerosol chemistry, and
268 inversion of methane satellite data where GEOS-Chem provides the forward model. The 12-km
269 simulation has stronger vertical transport (up to 20% decrease in ^{222}Rn surface concentrations)
270 because of improved representation of eddy fluxes. It shows finer spatial structure in surface
271 pollutants (NO_2), with improved capability to reproduce urban observations. It better represents
272 surface ozone titration in urban air and slightly increases the surface ozone background by
273 increasing vertical transport. Application to the Integrated Methane Inversion (IMI) shows
274 regional-scale results consistent with a 25-km inversion but higher information content and
275 greater spatial detail.

276

277



278 **Code and data availability.**

279 The source code of GEOS-Chem version 14.6.0 is publicly available at
280 <https://doi.org/10.5281/zenodo.15243271>. The GEOS-FP meteorological fields used to drive
281 GEOS-Chem are available on the Amazon Web Services (AWS) cloud
282 (<https://s3.amazonaws.com/gcgrid/index.html>; last access: 28 October 2024).

283

284 **Author contributions.**

285 XW and DJJ conceptualized the research. XW performed the analyses and data visualization.
286 XW and MPS developed the model code. MPS, YZ and RVM contributed to the data collection.
287 XW and DJJ wrote the manuscript with input from all authors.

288

289 **Competing interests.**

290 The authors declare no competing interests.

291

292 **Financial support.** This research has been supported by the United Nations Environment
293 Programme's International Methane Emissions Observatory (IMEO) and by the NASA
294 Atmospheric Composition Modeling and Analysis Program (grant no. 80NSSC23K0926). RVM
295 acknowledges support from the U.S. National Science Foundation (NSF; grant no. 2244984).

296

297

298

299 **References**

300 Bruno, J. H., Jacob, D. J., Wang, X., Sulprizio, M. P., Estrada, L. A., Varon, D. V., Wofsy, S. C.,
301 Omara, M., and Gautam, R.: Integrating MethaneAIR aircraft and TROPOMI satellite
302 observations in the Integrated Methane Inversion (IMI) to optimize methane emissions,
303 submitted, 2025.

304 Bey, I., Jacob, D. J., Yantosca, R. M., Logan, J. A., Field, B. D., Fiore, A. M., Li, Q., Liu, H. Y.,
305 Mickley, L. J., and Schultz, M. G.: Global modeling of tropospheric chemistry with assimilated
306 meteorology: Model description and evaluation, *J. Geophys. Res. Atmospheres*, 106, 23073–
307 23095, <https://doi.org/10.1029/2001JD000807>, 2001.

308 Bindle, L., Martin, R. V., Cooper, M. J., Lundgren, E. W., Eastham, S. D., Auer, B. M., Clune, T.
309 L., Weng, H., Lin, J., Murray, L. T., Meng, J., Keller, C. A., Putman, W. M., Pawson, S., and



310 Jacob, D. J.: Grid-stretching capability for the GEOS-Chem 13.0.0 atmospheric chemistry
311 model, *Geosci. Model Dev.*, 14, 5977–5997, <https://doi.org/10.5194/gmd-14-5977-2021>, 2021.

312 Brasseur, G. P. and Jacob, D. J.: *Modeling of Atmospheric Chemistry*, 1st ed., Cambridge
313 University Press, <https://doi.org/10.1017/9781316544754>, 2017.

314 Eastham, S. D., Long, M. S., Keller, C. A., Lundgren, E., Yantosca, R. M., Zhuang, J., Li, C.,
315 Lee, C. J., Yannetti, M., Auer, B. M., Clune, T. L., Kouatchou, J., Putman, W. M., Thompson, M.
316 A., Trayanov, A. L., Molod, A. M., Martin, R. V., and Jacob, D. J.: GEOS-Chem High
317 Performance (GCHP v11-02c): a next-generation implementation of the GEOS-Chem chemical
318 transport model for massively parallel applications, *Geosci. Model Dev.*, 11, 2941–2953,
319 <https://doi.org/10.5194/gmd-11-2941-2018>, 2018.

320 Estrada, L. A., Varon, D. J., Sulprizio, M., Nesser, H., Chen, Z., Balasus, N., Hancock, S. E., He,
321 M., East, J. D., Mooring, T. A., Oort Alonso, A., Maasakkers, J. D., Aben, I., Baray, S., Bowman,
322 K. W., Worden, J. R., Cardoso-Saldaña, F. J., Reidy, E., and Jacob, D. J.: Integrated Methane
323 Inversion (IMI) 2.0: an improved research and stakeholder tool for monitoring total methane
324 emissions with high resolution worldwide using TROPOMI satellite observations, *Geosci. Model
325 Dev.*, 18, 3311–3330, <https://doi.org/10.5194/gmd-18-3311-2025>, 2025.

326 Hancock, S. E., Jacob, D. J., Chen, Z., Nesser, H., Davitt, A., Varon, D. J., Sulprizio, M. P.,
327 Balasus, N., Estrada, L. A., Cazorla, M., Dawidowski, L., Diez, S., East, J. D., Penn, E., Randles,
328 C. A., Worden, J., Aben, I., Parker, R. J., and Maasakkers, J. D.: Satellite quantification of
329 methane emissions from South American countries: a high-resolution inversion of TROPOMI
330 and GOSAT observations, *Atmospheric Chem. Phys.*, 25, 797–817, <https://doi.org/10.5194/acp-25-797-2025>, 2025.

332 Kim, P. S., Jacob, D. J., Fisher, J. A., Travis, K., Yu, K., Zhu, L., Yantosca, R. M., Sulprizio, M.
333 P., Jimenez, J. L., Campuzano-Jost, P., Froyd, K. D., Liao, J., Hair, J. W., Fenn, M. A., Butler, C.
334 F., Wagner, N. L., Gordon, T. D., Welti, A., Wennberg, P. O., Crounse, J. D., St. Clair, J. M.,
335 Teng, A. P., Millet, D. B., Schwarz, J. P., Markovic, M. Z., and Perring, A. E.: Sources,
336 seasonality, and trends of southeast US aerosol: an integrated analysis of surface, aircraft, and
337 satellite observations with the GEOS-Chem chemical transport model, *Atmospheric Chem.
338 Phys.*, 15, 10411–10433, <https://doi.org/10.5194/acp-15-10411-2015>, 2015.

339 Lin, H., Jacob, D. J., Lundgren, E. W., Sulprizio, M. P., Keller, C. A., Fritz, T. M., Eastham, S.
340 D., Emmons, L. K., Campbell, P. C., Baker, B., Saylor, R. D., and Montuoro, R.: Harmonized
341 Emissions Component (HEMCO) 3.0 as a versatile emissions component for atmospheric
342 models: application in the GEOS-Chem, NASA GEOS, WRF-GC, CESM2, NOAA GEFS-
343 Aerosol, and NOAA UFS models, *Geosci. Model Dev.*, 14, 5487–5506,
344 <https://doi.org/10.5194/gmd-14-5487-2021>, 2021.

345 Lin, J.-T. and McElroy, M. B.: Impacts of boundary layer mixing on pollutant vertical profiles in
346 the lower troposphere: Implications to satellite remote sensing, *Atmos. Environ.*, 44, 1726–1739,
347 <https://doi.org/10.1016/j.atmosenv.2010.02.009>, 2010.

348 Liu, H., Jacob, D. J., Bey, I., and Yantosca, R. M.: Constraints from 210Pb and 7Be on wet
349 deposition and transport in a global three-dimensional chemical tracer model driven by



350 assimilated meteorological fields, *J. Geophys. Res. Atmospheres*, 106, 12109–12128,
351 <https://doi.org/10.1029/2000JD900839>, 2001.

352 Lu, X., Hong, J., Zhang, L., Cooper, O. R., Schultz, M. G., Xu, X., Wang, T., Gao, M., Zhao, Y.,
353 and Zhang, Y.: Severe surface ozone pollution in china: A global perspective, *Environ. Sci.*
354 *Technol. Lett.*, 5, 487–494, <https://doi.org/10.1021/acs.estlett.8b00366>, 2018.

355 Maasakkers, J. D., McDuffie, E. E., Sulprizio, M. P., Chen, C., Schultz, M., Brunelle, L., Thrush,
356 R., Steller, J., Sherry, C., Jacob, D. J., Jeong, S., Irving, B., and Weitz, M.: A gridded inventory
357 of annual 2012–2018 U.S. anthropogenic methane emissions, *Environ. Sci. Technol.*, 57, 16276–
358 16288, <https://doi.org/10.1021/acs.est.3c05138>, 2023.

359 Martin, R. V., Eastham, S. D., Bindle, L., Lundgren, E. W., Clune, T. L., Keller, C. A., Downs,
360 W., Zhang, D., Lucchesi, R. A., Sulprizio, M. P., Yantosca, R. M., Li, Y., Estrada, L., Putman, W.
361 M., Auer, B. M., Trayanov, A. L., Pawson, S., and Jacob, D. J.: Improved advection, resolution,
362 performance, and community access in the new generation (version 13) of the high-performance
363 GEOS-Chem global atmospheric chemistry model (GCHP), *Geosci. Model Dev.*, 15, 8731–8748,
364 <https://doi.org/10.5194/gmd-15-8731-2022>, 2022.

365 Philip, S., Martin, R. V., and Keller, C. A.: Sensitivity of chemistry-transport model simulations
366 to the duration of chemical and transport operators: a case study with GEOS-Chem v10-01,
367 *Geosci. Model Dev.*, 9, 1683–1695, <https://doi.org/10.5194/gmd-9-1683-2016>, 2016.

368 Varon, D. J., Jacob, D. J., Sulprizio, M., Estrada, L. A., Downs, W. B., Shen, L., Hancock, S. E.,
369 Nesser, H., Qu, Z., Penn, E., Chen, Z., Lu, X., Lorente, A., Tewari, A., and Randles, C. A.:
370 Integrated Methane Inversion (IMI 1.0): a user-friendly, cloud-based facility for inferring high-
371 resolution methane emissions from TROPOMI satellite observations, *Geosci. Model Dev.*, 15,
372 5787–5805, <https://doi.org/10.5194/gmd-15-5787-2022>, 2022.

373 Wang, X., Jacob, D. J., Downs, W., Zhai, S., Zhu, L., Shah, V., Holmes, C. D., Sherwen, T.,
374 Alexander, B., Evans, M. J., Eastham, S. D., Neuman, J. A., Veres, P. R., Koenig, T. K.,
375 Volkamer, R., Huey, L. G., Bannan, T. J., Percival, C. J., Lee, B. H., and Thornton, J. A.: Global
376 tropospheric halogen (Cl, Br, I) chemistry and its impact on oxidants, *Atmospheric Chem. Phys.*,
377 21, 13973–13996, <https://doi.org/10.5194/acp-21-13973-2021>, 2021.

378 Wang, Y. X., McElroy, M. B., Jacob, D. J., and Yantosca, R. M.: A nested grid formulation for
379 chemical transport over Asia: Applications to CO, *J. Geophys. Res. Atmospheres*, 109,
380 <https://doi.org/10.1029/2004JD005237>, 2004.

381 Wecht, K. J., Jacob, D. J., Frankenberg, C., Jiang, Z., and Blake, D. R.: Mapping of North
382 American methane emissions with high spatial resolution by inversion of SCIAMACHY satellite
383 data, *J. Geophys. Res. Atmospheres*, 119, 7741–7756, <https://doi.org/10.1002/2014JD021551>,
384 2014.

385 Yu, K., Keller, C. A., Jacob, D. J., Molod, A. M., Eastham, S. D., and Long, M. S.: Errors and
386 improvements in the use of archived meteorological data for chemical transport modeling: an
387 analysis using GEOS-Chem v11-01 driven by GEOS-5 meteorology, *Geosci. Model Dev.*, 11,
388 305–319, <https://doi.org/10.5194/gmd-11-305-2018>, 2018.



389 Zhai, S., Jacob, D. J., Wang, X., Shen, L., Li, K., Zhang, Y., Gui, K., Zhao, T., and Liao, H.: Fine
390 particulate matter (PM_{2.5}) trends in China, 2013–2018: separating contributions from
391 anthropogenic emissions and meteorology, *Atmospheric Chem. Phys.*, 19, 11031–11041,
392 https://doi.org/10.5194/acp-19-11031-2019, 2019.

393 Zhai, S., Jacob, D. J., Brewer, J. F., Li, K., Moch, J. M., Kim, J., Lee, S., Lim, H., Lee, H. C.,
394 Kuk, S. K., Park, R. J., Jeong, J. I., Wang, X., Liu, P., Luo, G., Yu, F., Meng, J., Martin, R. V.,
395 Travis, K. R., Hair, J. W., Anderson, B. E., Dibb, J. E., Jimenez, J. L., Campuzano-Jost, P., Nault,
396 B. A., Woo, J.-H., Kim, Y., Zhang, Q., and Liao, H.: Relating geostationary satellite
397 measurements of aerosol optical depth (AOD) over East Asia to fine particulate matter (PM_{2.5}):
398 insights from the KORUS-AQ aircraft campaign and GEOS-Chem model simulations,
399 *Atmospheric Chem. Phys.*, 21, 16775–16791, https://doi.org/10.5194/acp-21-16775-2021, 2021.

400 Zhang, L., Liu, L., Zhao, Y., Gong, S., Zhang, X., Henze, D. K., Capps, S. L., Fu, T.-M., Zhang,
401 Q., and Wang, Y.: Source attribution of particulate matter pollution over North China with the
402 adjoint method, *Environ. Res. Lett.*, 10, 084011, https://doi.org/10.1088/1748-9326/10/8/084011,
403 2015.

404 Zheng, B., Tong, D., Li, M., Liu, F., Hong, C., Geng, G., Li, H., Li, X., Peng, L., Qi, J., Yan, L.,
405 Zhang, Y., Zhao, H., Zheng, Y., He, K., and Zhang, Q.: Trends in China's anthropogenic
406 emissions since 2010 as the consequence of clean air actions, *Atmospheric Chem. Phys.*, 18,
407 14095–14111, https://doi.org/10.5194/acp-18-14095-2018, 2018.

408 Zhuang, J., Jacob, D. J., Gaya, J. F., Yantosca, R. M., Lundgren, E. W., Sulprizio, M. P., and
409 Eastham, S. D.: Enabling Immediate Access to Earth Science Models through Cloud Computing:
410 Application to the GEOS-Chem Model, *Bull. Am. Meteorol. Soc.*, 100, 1943–1960,
411 https://doi.org/10.1175/BAMS-D-18-0243.1, 2019.

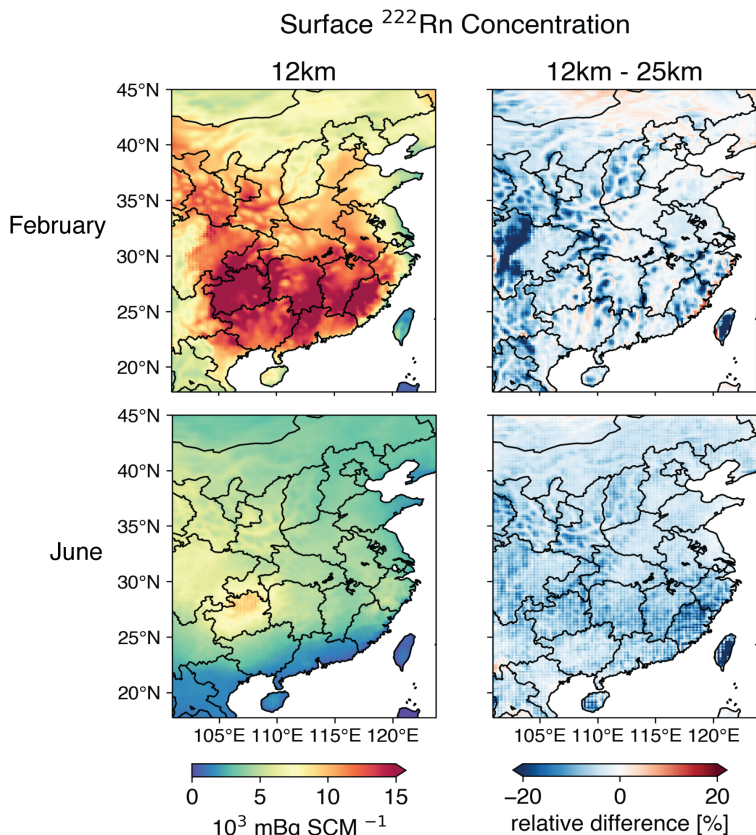
412 US Census Bureau, TIGER/Line Shapefile, 2017, 2010 nation, U.S., 2010 Census Urban Area
413 National. <https://catalog.data.gov/dataset/tiger-line-shapefile-2017-2010-nation-u-s-2010-census-urban-area-national>. Deposited 1 August 2019.

415

416



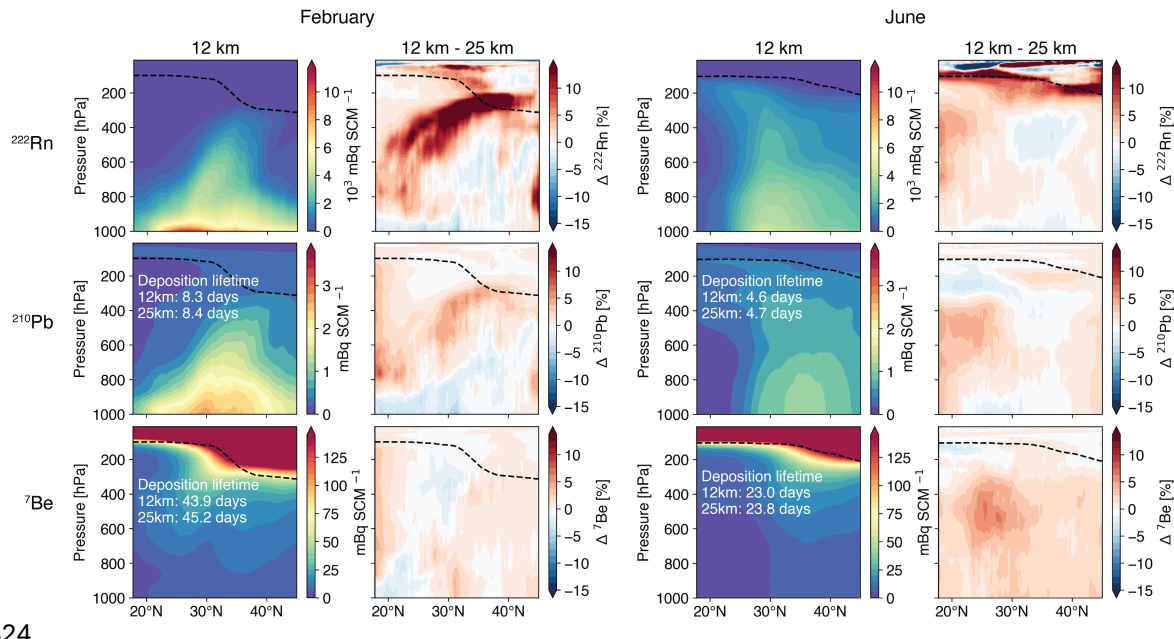
417



418 **Figure 1.** Monthly mean surface ^{222}Rn mixing ratios (mBq SCM^{-1}) over China simulated by
419 GEOS-Chem at 12-km resolution, and relative differences with a simulation at 25-km resolution,
420 for February and June 2022. SCM is a standard cubic meter of air at 0 °C (273.15 K) and 1 atm
421 (1013.25 hPa).

422

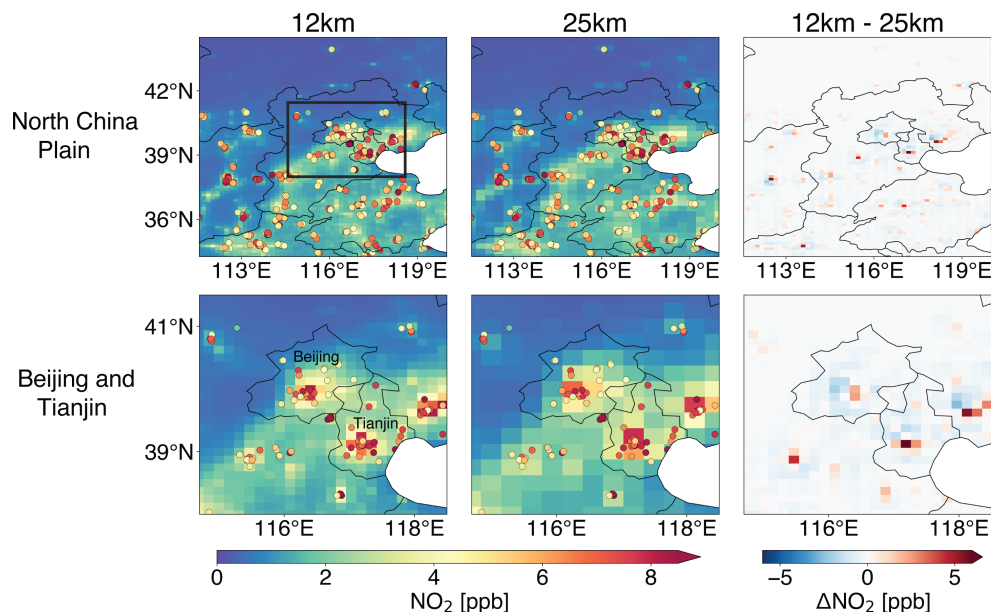
423



425 **Figure 2.** Zonally averaged latitude-pressure monthly mean mixing ratios of ^{222}Rn , ^{210}Pb , and
 426 ^{7}Be simulated by GEOS-Chem at 12-km resolution, and relative differences with a 25-km
 427 simulation, for February and June 2022 over China (domain of Figure 1). Lifetimes of
 428 tropospheric ^{210}Pb and ^{7}Be against deposition are inset. The dashed black lines indicate the
 429 tropopause.



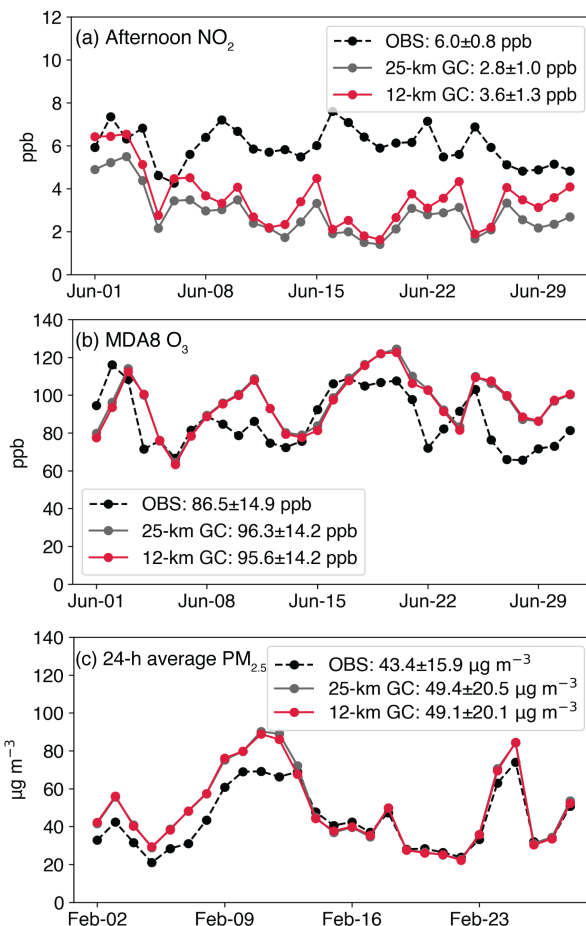
431



432

433 **Figure 3.** Afternoon (13–18 local time) monthly mean surface NO_2 concentrations in June 2022
434 simulated by GEOS-Chem at 12-km and 25-km resolution, for the North China Plain (NCP) and
435 for Beijing and Tianjin (box in top left panel). Circles show CNEMC network observations.

436



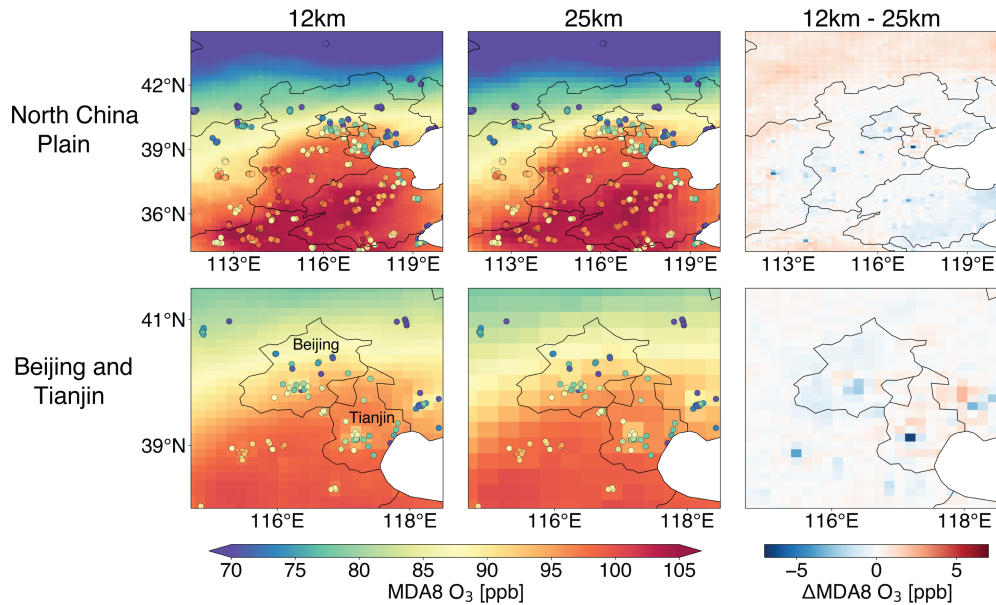
437

438

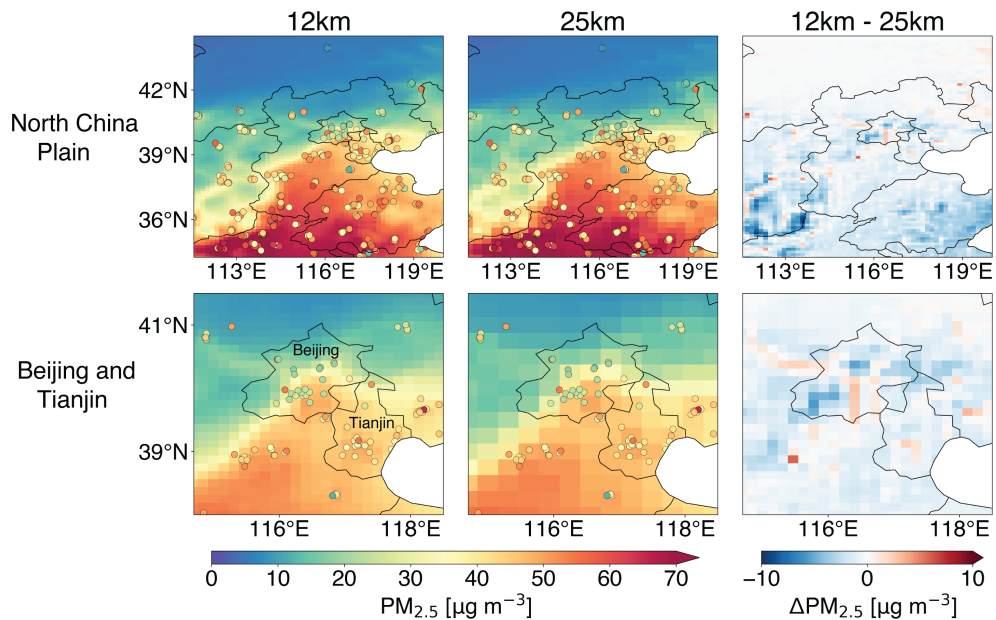
439 **Figure 4.** Daily time series of surface concentrations in the North China Plain (NCP): (a)
440 afternoon (13–18 local time) NO_2 in June 2022, (b) maximum daily 8-h average (MDA8) ozone
441 in June 2022, and (c) 24-h average $\text{PM}_{2.5}$ in February 2022. Observations at China National
442 Environmental Monitoring Center (CNEMC) sites, shown as circles in Figure 3 and averaged
443 over the NCP domain, are compared to GEOS-Chem simulations at 12- and 25-km resolution for
444 the same sites. Monthly mean values and standard deviations across all domain sites are shown
445 inset.

446

447



448 **Figure 5.** Same as Figure 3 but for surface MDA8 ozone concentrations in June 2022.

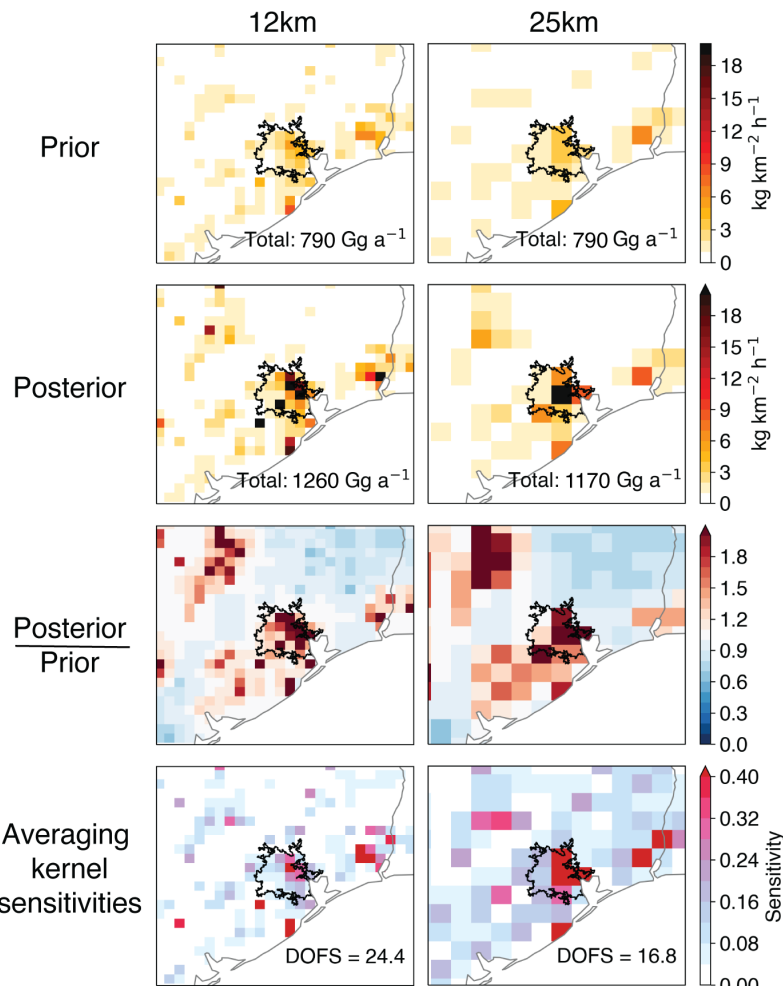


449

450 **Figure 6.** Same as Figure 3 but for surface 24-h average PM_{2.5} concentrations in February 2022.

451

452



453

454 **Figure 7.** Methane emissions in the Houston area of eastern Texas ($3^\circ \times 4^\circ$ domain) inferred from
455 TROPOMI satellite observations using the Integrated Methane Inversion (IMI) at 12- and 25-km
456 resolution. Panels from top to bottom are prior emissions from bottom-up inventories; posterior
457 emissions from the inversion; ratio of posterior to prior emissions; and averaging kernel
458 sensitivities that quantify the sensitivity of the posterior estimates to the true state. The Houston
459 urban boundary (US Census Bureau, 2017) is delineated in black. Emission totals over the whole
460 $3^\circ \times 4^\circ$ domain are shown inset in the top two rows. The sum of area-weighted averaging kernel
461 sensitivities for the whole domain defines the Degrees of Freedom for Signal (DOFS) inset in the
462 bottom panels.